Achieving superior electromagnetic wave absorbers through the novel metal-organic frameworks derived magnetic porous carbon nanorods

Nannan Wu [a, c], Dongmei Xu [a, b], Zhou Wang [a], Fenglong Wang [a], Jiurong Liu [a, *], Wei Liu [b], Qian Shao [d], Hu Liu [e], Qiang Gao [f], Zhanhu Guo [c]

[a] Key Laboratory for Liquid-Solid Structural Evolution and Processing of Materials, Ministry of Education and School of Materials Science and Engineering, Shandong University, Jinan, Shandong, 250061, China
[b] State Key Laboratory of Crystal Materials, Shandong University, Shandong, 250100, China
[c] Integrated Composites Laboratory (ICL), Department of Chemical & Biomolecular Engineering, University of Tennessee, Knoxville, TN, 37996, USA
[d] College of Chemical and Environmental Engineering, Shandong University of Science and Technology, Qingdao, 266590, China
[e] National Engineering Research Center for Advanced Polymer Processing Technology, Zhengzhou University, Zhengzhou, 450002, China
[f] Center for Nanophase Materials Sciences, Oak Ridge National Laboratory, P. O. Box 2008, Oak Ridge, TN, 37831, USA

ARTICLE INFO

ABSTRACT

High absorption capacity and broad absorption bandwidth electromagnetic wave (EMW) absorption materials (namely, EMW absorbers) are highly desirable due to the interference with electronics and harms on human beings' health. In search for rational design on nanostructured absorbers, we have synthesized and demonstrated the rod-shape composites with Fe-containing magnetic nanoparticles (Fe_3O_4, Fe_3C and Fe NPs) embedded into nano-porous carbon (NPC) through pyrolysis of Fe-based metal-organic frameworks (MOFs). The morphologies, compositions, and graphitization degree of the Fe-MOFs derived magnetic NPC nanorods can be effectively controlled via adjusting the pyrolysis temperatures. The graphitization level has a significant influence on the permittivity of the composites upon variation of pyrolysis temperatures, thereby a tunable electromagnetic wave (EMW) absorption is observed. Consequently, the resulting magnetic NPC nanorods obtained at pyrolysis temperature of 600 and 700 °C exhibit the most remarkable EMW absorption performance with a strong reflection loss of −52.9 dB and broad effective bandwidth (f_e) of 4.64 GHz at 3.07 mm. With a thickness of 3.5 mm, the f_e for the magnetic NPC nanorods at 600 °C covers the whole X-band from 7.92 to 12.48 GHz. The noticeable EMW absorption performances have been greatly enhanced compared to those reported Fe_3O_4 based absorbers, owing to the synergy of multiple components and the porous structures inherited from MOFs.

© 2019 Published by Elsevier Ltd.

1. Introduction

The rapid penetration of portable electronics and wireless communication technology has required our society to tackle the issues from the unwanted electromagnetic wave (EMW) pollution [1—6]. It is well accepted that the most effective approach to address EMW interference is to develop high performance EMW absorbing materials. Hence extensive attempts have been made to synthesize EMW absorbers, emphasizing the characteristics of low reflection values, thin thickness, broad effective frequency bandwidth, and light weight [7—9]. Based on the loss mechanism of the

EM energy, the absorbers could be divided into three categories: the dielectric, magnetic, and resistance loss types [10]. Generally, dielectric loss materials own a strong absorbing intensity, while the broad frequency range cannot be easy to reach due to their unbalanced impedance matching, limited loss mechanisms, etc [11]. Amongst the dielectric materials, a variety of carbons have been the competitive EMW absorbers owing to their low density, strong dielectric loss, natural abundance, and excellent chemical stability [12—14]. Various carbons including carbon nanofibers [15], graphene [16], and carbon nanotubes (CNTs) [17] have been at the forefront for EMW absorbers. Nevertheless, carbon materials are unilateral dielectric materials with high permittivity value and no magnetism resulting in impedance mismatch. According to impedance matching conditions $Z_{in} = Z_0(\mu_r/\varepsilon_r)^{1/2}$ [18], to improve the impedance matching level between incident waves and free

space, it is of great importance to manipulate the relative permeability μ_r close to the relative permittivity ε_r.

There are two strategies to improve the impedance level of carbon-based EMW absorbing materials. One effective way is to increase the permeability value by incorporating magnetic particles, i.e. Fe, Co, Ni, Fe_3O_4, into carbon materials. On one hand, such composites can effectively enhance the EMW absorption capability of carbon owing to the synergy of magnetic loss and dielectric loss. On the other hand, this approach is capable of significantly reducing the density of magnetic materials because of light-weight of carbon materials. Carbon nanofibers incorporated with ferromagnetic metals have exhibited remarkable EMW absorption performances with a reflection loss (RL) below −20 dB from 4 to 18 GHz corresponding to a thicknesses of 1.1−5.0 mm [15]. Che et al. reported an obviously enhanced EMW absorption than pure CNT using Fe encapsulated CNT nanocomposite, attributing to the optimized EM parameters [19]. Another effective way to achieve impedance matching is to decrease the permittivity by introducing voids or pores into carbon materials. Typically, porous structures, with unique characteristics such as low density and large surface area, would be a promising candidate as light weight EMW absorbers [20,21]. Besides, the massive pores can act as polarization centers, and can further enhance the dielectric loss ability by inducing polarization relaxations [11,12]. For example, porous Fe particles showed stronger EMW absorption ability than the non-porous structure due to the multi-polarizations induced by the porous structure [22]. Fang et al. reported that the porous carbon foams owned smaller dielectric constants but several times larger dielectric loss than their corresponding compact powders [23]. Hence, the fabrication of porous structures is an effective method to modify EM parameters of absorbers. Thus, multiple-component absorbing materials obviously outperform the single component dielectric absorbers to reach the goal of increasing magnetic loss and improving impedance matching level. To date, the challenges are that the magnetic metals or ferrite particles tend to reunite at the nanoscale and the deliberate control over porous structures is quite difficult. Therefore, it is highly desirable to develop a facile and cost-effective approach to synthesize the composites of magnetic particles and porous carbon with uniform particle size and dispersion.

More recently, MOFs derived composites have been demonstrated to be the promising candidates for ideal absorbers [24−27]. On one hand, graphite carbon can be obtained with the catalysis role of metals during the pyrolysis process, thereby a strong dielectric-loss ability of the resulting materials [28−30]. On the other hand, a magnetic metal can deliver noticeable magnetic loss. The multi-component synergistic effects improve the impedance matching through combination of magnetic and dielectric loss, and achieve more interfaces to enhance the interfacial polarization [11]. Lu et al. reported excellent EMW absorption properties with a minimum RL of −35.3 dB at 2.5 mm for the porous Co/C nanocomposites via thermal decomposition of Co-MOFs [30]. Qiang et al. have fabricated porous Fe/C nano-cubes by pyrolyzing the Prussian blue, showing a broad absorption bandwidth 10.8−18.0 GHz with RL values exceeding −10 dB [31]. On the other and, Fe-based MOF materials are extremely attractive since Fe is an earth-abundant element and Fe-containing complexes have been widely investigated for EMW absorbers owing to their excellent magnetic properties, facile manipulation, and low cost [13,32−34]. To the best of our knowledge, porous magnetite-carbon nanocomposiets derived from MOFs, i.e., Fe-MIL-88A [35−37], for EMW absorbing materials has not been reported.

In this work, we demonstrated and synthesized a series of rod-shape composites with Fe-containing magnetic nanoparticles (Fe_3O_4, Fe_3C and Fe NPs) embedded into porous carbon through pyrolysis of Fe-MIL-88A. The structures, compositions, and magnetic properties of the composites obtained at pyrolysis temperature ranges of 500−800 °C were investigated. The compositions of the magnetic NPC nanorods significantly affected the magnetic properties and the graphitization degree was found to have a great influence on the permittivity of the composites with the variation of pyrolysis temperatures. Consequently, the EMW absorption performances of the resulting magnetic NPC nanorods could be tuned easily through changing the pyrolysis temperatures. The EMW absorption performances for the magnetic NPC nanorods obtained at 600 °C outperformed pure Fe_3O_4 and previously reported Fe_3O_4/C EMW absorbers. We thoroughly elucidated the contributions of synergistic effects from multi-components and high porosity inherited from MOFs on the enhanced EMW absorption.

2. Experimental

2.1. Preparation of Fe-MIL-88A and Fe-MIL-88A derived magnetic NPC nanorods

The hexagonal rod-shape Fe-MIL-88A was first prepared through a facile hydrothermal process according to a previous report with slight modifications [35]. Typically, 1 mmol $FeCl_3 \cdot 6H_2O$ was dissolved in 20 mL deionized water at room temperature firstly. Then 1 mmol fumaric acid was added into the above solution. After stirred for 0.5 h, the resulting solution was transferred into a Teflon-lined stainless-steel autoclave with a capacity of 30 mL and sealed to heat at 110 °C for 10 h. The obtained yellow products were washed with deionized water and dried under vacuum for 12 h. Then, the magnetic NPC nanorods were obtained by calcinating the Fe-MIL-88A precursor in a tube furnace under nitrogen flow at 500-800 °C for 5 h with a heating rate of 1 °C min^{-1}. The obtained products under different pyrolysis temperatures were defined as sample F5, F6, F7 and F8, respectively.

2.2. Preparation of samples for EMW measurements

For EMW absorption measurements, the samples were prepared by homogeneously mixing the magnetic NPC nanorods into epoxy resin with a filling content of 40 wt%. Then the mixture was cut into toroidal shaped samples (Φ_{out}: 7.00 mm, Φ_{in}: 3.04 mm).

2.3. Characterization

The X-ray powder diffraction (XRD) of the magnetic NPC nanorods was recorded on an X-ray diffraction (XRD) instrument with Cu K radiation ($\lambda = 0.15406$ nm, 40 kV, 40 mA). The morphology and microstructures were characterized by a field emission scanning electron microscope (FESEM, JSM-7500F, JEOL) and a JEOL JEM-2100 transmission electron microscope (TEM). The specific surface area was analyzed using Brunner-Emmet-Teller method. For the EM measurement, a vector network analyzer (VNA, Agilent PNA N5244A) was used to measure the scattering (S) parameters in 2−18 GHz. Then the complex permeability (μ_r) and complex permittivity (ε_r) were calculated from the measured S parameters using the software (Agilent Technologies 85071) installed in the VNA.

3. Results and discussions

Our synthesis route of the magnetic NPC nanorods is described in Fig. 1a. The Fe-MIL-88A was prepared using $FeCl_3 \cdot 6H_2O$ and fumaric acid in an aqueous solution. The SEM images of the Fe-MOFs precursor [Fig. S1a (see supporting information) and
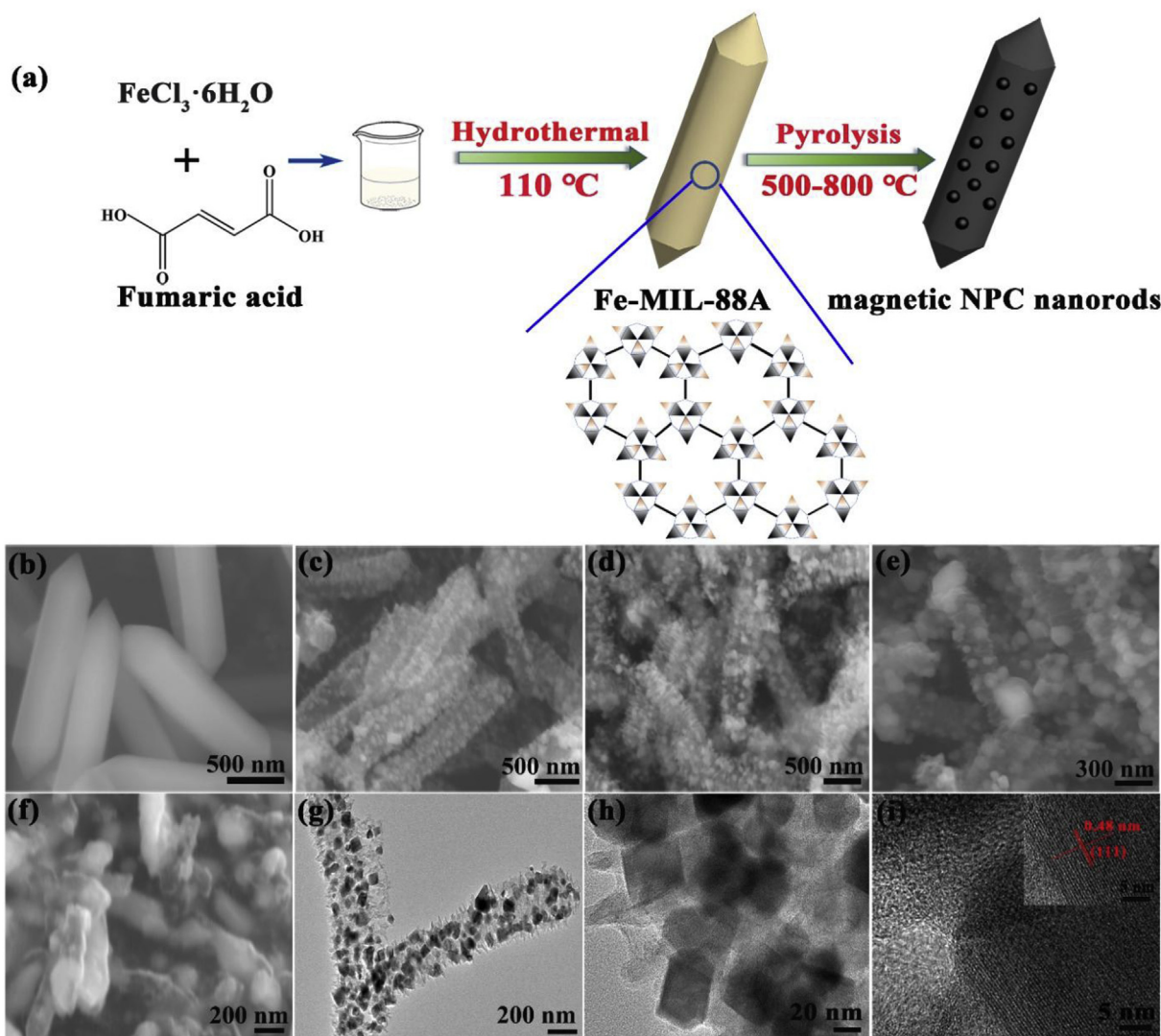
Fig. 1. (a) Synthetic process of magnetic NPC nanorods. SEM images of (b) Fe-MOFs (Fe-MIL-88A) precursor, and (c-f) Fe-MIL-88A derived magnetic NPC nanorods obtained at different pyrolysis temperatures under N_2 flow: (c) F5, (d) F6, (e) F7, and (f) F8. (g), (h) TEM images and (i) HR-TEM images of sample F6. (A colour version of this figure can be viewed online.)

Fig. 1b] show well-defined hexagonal rod-like morphology with a length of $1.0-1.5$ μm and width of ca. 300 nm. After the pyrolysis under N_2, the samples F5, F6, and F7 display quite rough and wrinkled surfaces compared with the Fe-MOFs precursor (see also Figs. S1b−d). In larger magnification images (Fig. 1c, d and e), numerous magnetic nanoparticles are observed to disperse uniformly on the carbon framework. Furthermore, the morphology of the magnetic NPC nanorods depends clearly on the pyrolysis temperatures. With increasing the temperature, the particle size becomes larger and the original structure tends to shrink and aggregate more remarkably. Up to 800 °C, the whole structure collapses and aggregates, resulting in the formation of irregular morphology (Fig. 1f). TEM and HR-TEM have been further employed to obtain the detailed structural information. Taking F6 as an example, the TEM images (Fig. 1g and h) present a porous rod-like morphology with Fe_3O_4 nanoparticles uniformly embedded in the amorphous carbon matrix. The length of magnetic NPC nanorods is ca. 1.2 μm and the diameter of the Fe_3O_4 nanoparticles shows a distribution between 25 and 50 nm. The HR-TEM images (Fig. 1i) of the particles suggest the lattice fringe of 0.254 nm fitted well with

(311) plane of the crystalline cubic spinel Fe_3O_4. From SAED image (Fig. S2), the diffraction rings correspond well with (111), (220), (311), (400), (422) and (511) planes of Fe_3O_4 [13]. Consequently, the magnetic NPC nanorods with Fe_3O_4 nanoparticles uniformly embedded into porous carbon matrix have been successfully fabricated by adopting the facile Fe-MOFs derived methodology.

Fig. S3 shows the XRD pattern of Fe-MIL-88A and it agrees well with previous reports [35,36]. The XRD patterns have been further utilized to characterize the structural information of the magnetic NPC nanorods (Fig. 2a). Sample F5, F6, and F7 were observed to display six peaks at 30.06°, 35.4°, 43.02°, 53.14°, 57.86°, and 62.76°, assigned to the (220), (311), (400), (422), (511) and (440) planes of the face-centered cubic structure Fe_3O_4 (JCPDS No. 19-0629), in good agreement with HRTEM analysis. Particularly, the diffraction peak intensity becomes stronger with the increase of pyrolysis temperature, implying the improved crystallinity of Fe_3O_4 particles. No other diffraction peaks are present, suggesting a high purity for the magnetic NPC nanorods. Up to 800 °C, most of the Fe^{3+} is reduced to Fe along with small amount of Fe_3C (JCPDS No. 35-0772). Meanwhile, no diffraction peaks of carbon could be detected,
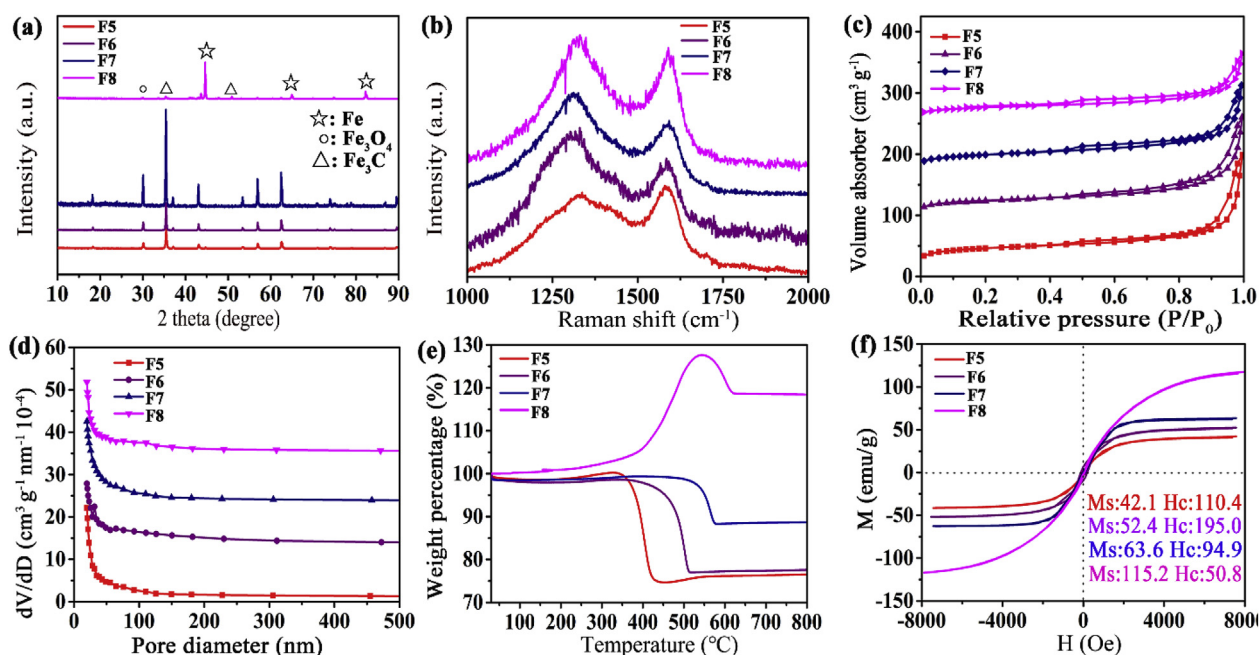
Fig. 2. (a) XRD patterns, (b) Raman spectra, (c) nitrogen adsorption-desorption isotherms, (d) pore size distributions, (e) TG curves under air and (f) room temperature magnetic hysteresis loops of the magnetic NPC nanorods obtained at different pyrolysis temperatures under N_2 flow. (A colour version of this figure can be viewed online.)

suggesting the porous carbon exists in an amorphous state. The average grain sizes of sample F5, F6, F7, F8 are calculated to be 31.2, 49.0, 83.3 and 93.8 nm, respectively, by applying the Scherrer's equation [16], in accordance with the SEM observations in Fig. 1.

In addition, the pyrolysis condition such as heating rate has a great impact on the compositions of the resultant products. If we increased the rate from 1 to 5 °C min and maintained at 500 °C with the heating time unchanged, the XRD patterns of the magnetic NPC nanorods display characteristic peaks assigned to FeO (Fig. S4), which will weaken the magnetic loss ability of the composites. The presence of FeO should be associated with the reaction of Fe^{3+} and carbon during the pyrolysis of MOFs, and a fast heating rate of 5 °C min^{-1} could promote the reduction of Fe^{3+} to Fe^{2+} by carbon. Similarly, the diffraction peaks of CoO could be observed in the XRD patterns of MOFs derived Co/C composites when adopting the heating rate of 5 °C min^{-1} while high purity Co was obtained with a low heating rate of 1 °C min^{-1} [24]. The results show that a rational pyrolysis condition has a good control over the compositions and purity of the MOFs derived products. These results indicate that pyrolyzing at 1 °C min^{-1} is a better condition to obtain high purity Fe_3O_4/C composites. It is well-known that the graphitization has a great impact on the EMW absorption ability, therefore, the Raman analysis on the samples was carried out. Fig. 2b shows that all samples exhibit two typical peaks at ca. 1330 cm^{-1} (D band) and 1540 cm^{-1} (G band). According to previous reports [38,39], D band is related to the K-point phonons of A_{1g} mode and it becomes active with the presence of disorder graphite or nano-graphite crystals. The G band results from the scattering of the E_{2g} vibration mode, corresponding to the vibration of sp^2 carbon dominant in graphene nanosheets. Generally, the intensity ratio of the D band to the G band (I_D/I_G) is calculated as an index to evaluate the graphitization degree of carbon materials [40,41]. The I_D/I_G value for F5, F6, and F7 is 0.92, 1.31, and 1.37, respectively. The increased I_D/I_G value can be well explained by Ferrari and Robertson's theory [38], according to which the transformation of amorphous carbon to graphite could be divided into two stages. The first stage is amorphous carbon to nanocrystalline graphite and the second is nanocrystalline graphite

to graphite. The first one led to an increased I_D/I_G value as the defects in the nanocrystalline graphite would become active, while the second stage tended to cause a decreased I_D/I_G value owing to the elimination of defects. Therefore, an enhanced I_D/I_G value can be seen with increasing the temperature from 500 to 700 °C, suggesting the transformation of amorphous carbon to nanocrystalline graphite. To further verify this explanation, we also calculated the I_D/I_G value of the magnetic NPC nanorods pyrolyzed at 800 °C. A decreased I_D/I_G value of 1.08 in Fig. 2b further confirms the existence of the second stage. On the other hand, from the TEM images of F8 (Fig. S5), a noticeable lattice fringe of carbon outside of Fe nanoparticles was detected. The formation of graphite carbon should be mainly attributed to the catalysis effect of Fe during the pyrolysis process. These results confirm the gradually enhanced graphitization of the magnetic NPC nanorods accompanying with increasing the temperatures. Previous studies have proved that the graphitization degree has a noticeable effect on the permittivity and absorbing properties of the EMW absorbers [10,31]. A rather high graphitization degree will cause a largely enhanced permittivity, resulting in the impedance mismatch. Thus, an appropriate graphitization degree is a pre-requisite to obtain an excellent absorber.

The porosity of F5, F6, F7 and F8 has been monitored by BET analysis. As a result, all four samples present a characteristic IV-type isotherm (Fig. 2c), indicating the existence of mesopores with the dominant pore size of 19.8 nm (Fig. 2d) [42]. The BET specific surface area (m^2 g^{-1}) is 148.1 m^2 g^{-1} for F5, 121.1 m^2 g^{-1} for F6, 127.1 m^2 g^{-1} for F7, and 86.6 m^2 g^{-1} for F8, respectively. The decreased specific surface area for F8 should be attributed to the aggregation of particles and collapse of the structures, but the values are still larger than the reported Fe_3O_4/C composites including porous Fe_3O_4/C nanorods (45.2 m^2 g^{-1}) [43], Fe_3O_4/C nano-rings (64.27 m^2 g^{-1}) [13], mesoporous C-encapsulated Fe_3O_4 (51.72 m^2 g^{-1}) [44]. The large specific surface area and mesopores will be of great importance to suppress the eddy current effect and modify the permittivity of EMW absorbers [12]. To evaluate the weight percentage of carbon and Fe_3O_4 in the magnetic NPC

nanorods, the TGA measurements were carried out in air from room temperature to 800 °C, displayed in Fig. 2e. As carbon can be oxidized completely at 800 °C, the final product should be only Fe_2O_3. Then the content of carbon for sample F5, F6, F7 and F8 is calculated by using Equations (1) and (2), respectively:

$$wt\%_L = \frac{3(1 - wt\%_{carbon})}{2M_{Fe_3O_4}} \times M_{Fe_2O_3} \tag{1}$$

$$wt\%_L = \frac{(1 - wt\%_{carbon})}{2M_{Fe}} \times M_{Fe_2O_3} \tag{2}$$

where $wt\%_L$ is the weight percentage of left Fe_2O_3, and M represents the molecular weight of the corresponding chemicals. Then the weight percentage of carbon for F5, F6, F7 and F8 is confirmed to be 27.1%, 25.3%, 15.7% and 17.0%. The weight percentage of Fe_3O_4 for sample F5, F6, F7 is ca. 72.9%, 74.7%, 84.3% and the weight percentage of Fe for sample F8 is about 83.0%. Besides, it can be observed that the carbon content decreases at a high pyrolysis temperature of 700 and 800 °C and the reason can be ascribed to the formation of Fe_3C [31].

To characterize the magnetic properties of the samples, hysteresis loops of F5, F6, F7 and F8 were recorded using a vibrating sample magnetometer. The M_s value (emu g^{-1}) is increased from 42.1 of F5 to 52.4 of F6 and 63.6 of F7, 115.2 of F8 (Fig. 2f). The increments in M_s value are associated with the increased pyrolysis temperature, which promotes the growth and improves the crystallinity of Fe_3O_4 nanoparticles. However, the M_s value for F5, F6 and F7 is still much lower than the bulk Fe_3O_4 (92 emu g^{-1}) [43], attributing to the presence of non-magnetic carbon. The H_c value (Oe) of F5, F6, F7, F8 is 110.4, 195.0, 94.9 and 50.8, respectively (Fig. 2f). According to previous reports, H_c value owns a strong grain size dependent effect [45,46]. The H_c value increases to the maximum at the critical size and then decreases. Herein, the critical size of Fe_3O_4 (about 25 nm) is close to the grain size of F5 and F6 (shown in Fig. 1) [13], and much smaller than F7, F8, thus causing such a difference of H_c value.

The EMW absorption of an absorber is determined by the relative permittivity ($\varepsilon_r = \varepsilon' - j\varepsilon''$) and relative permeability ($\mu_r = \mu' - j\mu''$). Fig. 3 displays the changes of EM parameters for all samples with frequency. As displayed in Fig. 3a–d, the ε' value decreases from 4.8 to 3.4 for F5, 8.9 to 5.1 for F6 and 13.7 to 9.6 for F7 and 17.5 to 14.1 for F8, respectively. As for ε'', the resonance peaks (marked by circles) have been recorded for all samples (Fig. 3a–d) The ε' and ε'' can be described by the Debye Equations [47]:

$$\varepsilon' = \varepsilon_\infty + \frac{\varepsilon_s - \varepsilon_\infty}{1 + \omega^2\tau^2} \tag{3}$$

$$\varepsilon'' = \varepsilon''_p + \varepsilon''_c = (\varepsilon_s - \varepsilon_\infty)\omega\tau \Big/ \left(1 + \omega^2\tau^2\right) + \sigma/\omega\varepsilon_0 \tag{4}$$

in which ε_∞ refers to the relative permittivity at the high-frequency limit, ε_s is the static permittivity, τ is the polarization relaxation time, ω ($\omega = 2\pi f$) represents the angular frequency. According to Equation (3), the ε' is inversely proportional to frequency, thus showing a decreasing tendency with the increase of frequency. According to Equation (4), the ε'' is determined by the polarization loss (ε''_p) and conduction loss part (ε''_c). The conduction loss part should decrease as the frequency increases. However, the increased ε'' can be observed in a specific frequency range, as shown in Fig. 3a–d, indicating that the resonance peaks of ε'' are mainly caused by polarization loss. In order to further confirm the dielectric loss mechanisms for the magnetic NPC nanorods, the Debye theory is employed and the relationships between ε' and ε''

are illustrated as Equation (5) [47]:

$$[\varepsilon' - (\varepsilon_s + \varepsilon_\infty)/2]^2 + \left(\varepsilon''\right)^2 = [(\varepsilon_s - \varepsilon_\infty)/2]^2 \tag{5}$$

If ε' and ε'' satisfy Equation (5), then the plot of ε'' versus ε'' should present a semicircle which represents a Debye relaxation process [47]. Figs. S6a–d shows that sample F5, F6, F7 and F8 present a straight line firstly, indicating that conduction loss makes effect on dielectric loss [14]. Then several semicircles are observed, indicating the existence of polarization loss [48]. Basically, the polarization mechanisms can be further classified into interfacial polarization, dipolar polarization, ionic polarization, and electron polarization [48]. The ionic polarization and electron polarization can be easily excluded easily because they usually occur in much higher frequency region (10^3–10^6 GHz [48]). Therefore, the polarization mechanisms should be attributed to interfacial polarization and dipolar polarization. Herein, the polarization behaviors should be strongly associated with the special structure of the magnetic NPC nanorods. The magnetic NPC nanorods possess multiple interfaces of Fe_3O_4 (Fe)/carbon, carbon/epoxy resin. The space charges tend to accumulate at the heterointerfaces and produce dipole moments that lead to interfacial polarization [49,50]. On the other hand, the defects existed on the amorphous carbon framework are capable of functioning as polarization centers, generating polarization relaxations [51,52]. Additionally, the observed ε' and ε'' values are enhanced with the increase of pyrolysis temperatures. The improved graphitization degree of carbon with the increased pyrolysis temperatures (Fig. 2b) leads to a higher conductivity that contributes to enhanced permittivity on the basis of free electron theory. $\varepsilon = \frac{\sigma}{2\pi\varepsilon_0 f}$ [52].

Fig. 3e–h suggests that F8 owns the largest μ' values of all samples attributing to the strongest magnetism (Fig. 2g). With regard to the imaginary part μ'', all samples display similar values with the presence of several resonance peaks. As for the mechanisms of magnetic loss, natural resonance, exchange resonance, hysteresis loss and eddy current effect are widely accepted as the main causes [31]. Normally, the hysteresis loss often occurred in the weak field can be excluded [53]. The C_0 value representing the eddy current loss can be calculated by Equation (6) [54]:

$$C_0 = \mu''(\mu')^{-2f-1} = 2\pi\mu_0 d^2\sigma \tag{6}$$

where μ_0 is the permeability of vacuum, σ is the electric conductivity and d is the thickness of absorbers. C_0 should remain unchanged versus frequency if magnetic loss only arises from eddy current loss. Fig. S7 shows that the C_0 values of all four samples vary with frequency, indicating the magnetic loss should dominantly derive from natural resonance and exchange resonance. Aharoni put forward the theory that exchange resonance existed in the nanometer sized particles and Toneguzzo et al. concluded that the exchange resonance occurred at a higher frequency range than natural resonance [55,56]. Therefore, the resonance peaks in Fig. 3e–h between 2 and 6 GHz are attributed to natural resonance and the multi-resonance peaks in the frequency range of 10—18 GHz are ascribed to exchange resonance.

On the basis of the measured ε_r and μ_r, the RL values of the magnetic NPC nanorods are given using the transmission line theory [64]:

$$Z_{in} = Z_0(\mu_r/\varepsilon_r)^{1/2} \tanh\left\{j(2\pi fd/c)(\mu_r\varepsilon_r)^{1/2}\right\} \tag{7}$$

$$RL = 20 \, \log|(z_{in} - z_0)/(z_{in} + z_0)| \tag{8}$$

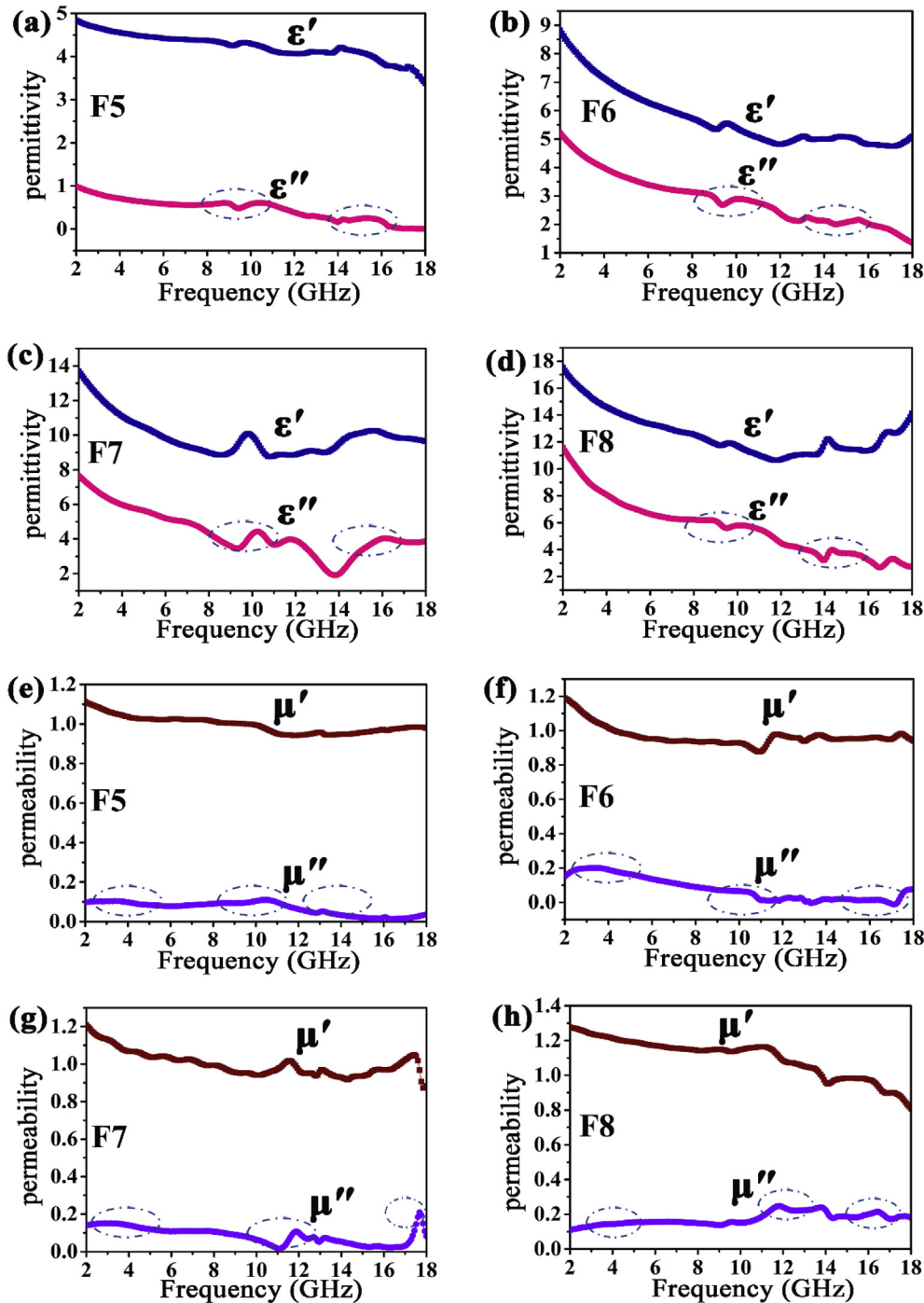in which Z_0 is the input impedance of free space, Z_{in} represents the

Fig. 3. Frequency dependence of complex permittivity for sample (a) F5, (b) F6, (c) F7 and (d) F8; frequency dependence of complex permeability for sample (e) F5, (f) F6, (g) F7 and (h) F8. (A colour version of this figure can be viewed online.)

input impedance of the absorber, f is the frequency, c is the light velocity, and d is the thickness of the magnetic NPC nanorods. Fig. 4 a, c, e, g shows the three-dimensional representation of RL values plotted against frequency in the thickness ranges of 1.0–5.0 mm for the magnetic NPC nanorods. Of all four samples, F5 shows the weakest EMW absorption intensity of only −7.9 dB at 10.68 GHz corresponding to a thickness of 3.65 mm (Fig. 4a). When the pyrolysis temperature is up to 600 and 700 °C, the optimal RL of F6 and F7 is −52.9 dB at 11.68 GHz with the thickness of 3.07 mm and −45.41 dB at 15.44 GHz corresponding a thickness of 1.58 mm

(Fig. 4c and e) and the effective absorption bandwidth (RL < −10 dB) can reach 4.64 GHz (9.44–14.08 GHz, Fig. 4d) for F6 and 3.12 GHz (14.48–17.6 GHz, Fig. 4f) for F7, respectively. With a thickness of 3.5 mm, the f_e of sample F6 covers the whole X band (8–12 GHz), which is of great significance for the design of radars. Wide absorption frequency ranges from 5.04 to 18.0 GHz for F6 and 3.92–18.0 GHz for F7 with RL < −10 dB can be obtained. When it comes to sample F8, the largely enhanced permittivity brings about a rather low RL of only −20.2 dB at 16.48 GHz (Fig. 4g). The more remarkable EMW absorption of F6 and F7 compared with F5 should
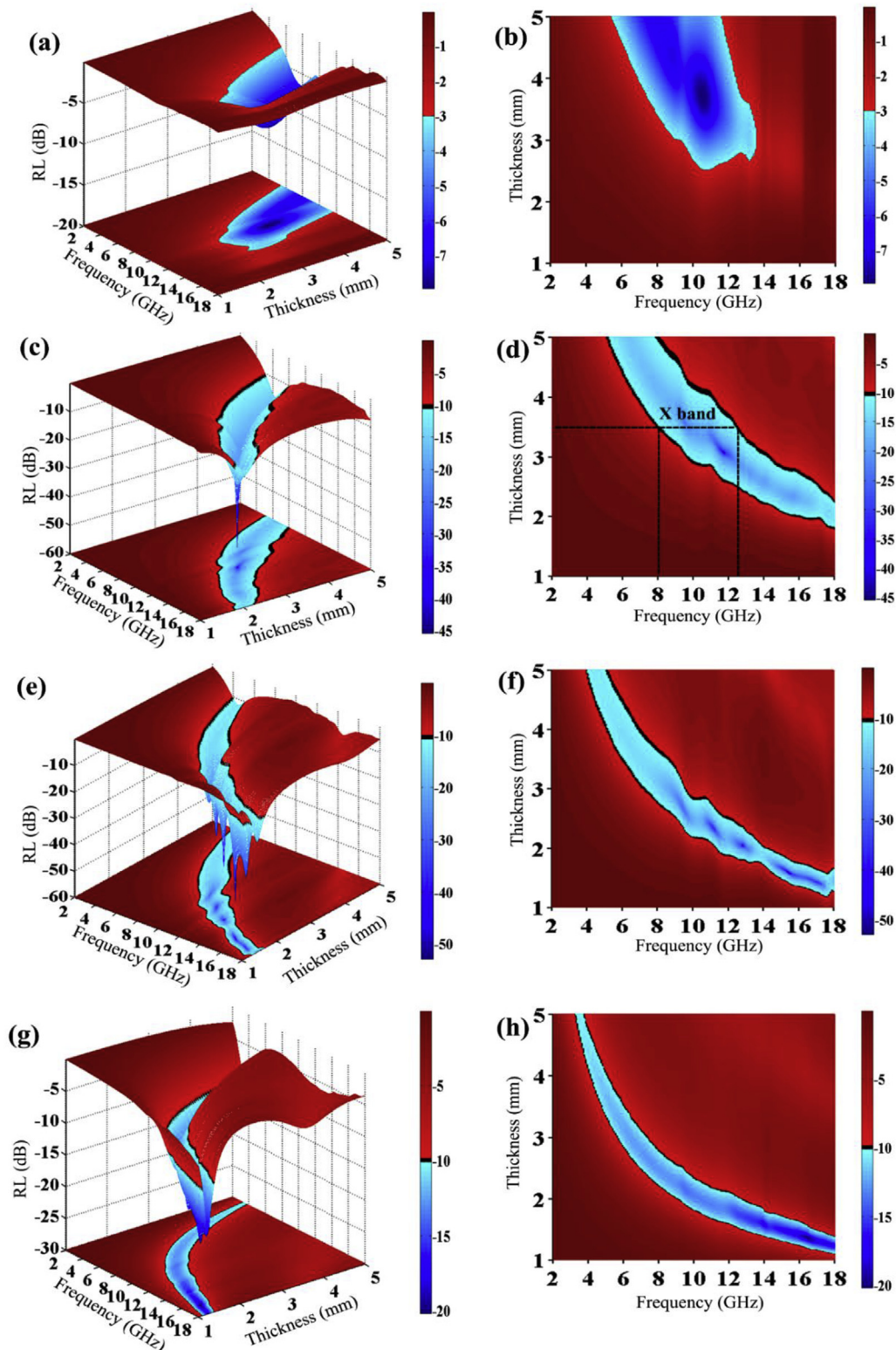
Fig. 4. 3D representations of RL values (a, c, e and g) and corresponding 2D contour plots (b, d, f, h) for sample (a, b) F5, (c, d) F6, (e, f) F7 and (g, h) F8. (A colour version of this figure can be viewed online.)

be attributed to the improved magnetic loss arising from the enhanced crystallinity of Fe_3O_4 nanoparticles and dielectric loss from increased graphitization degree of carbon. Nevertheless, too large permittivity of F8 leads to the mismatch between ε_r and μ_r, resulting in a weak absorption. Compared with previously reported

Fe_3O_4 based absorbers (Table 1), sample F6 and F7 also exhibit significantly enhanced EMW absorption at a low filling ratio. In contrast to those of MOFs-derived Co/C and Fe/C composites [30,31], the sample F6 displays much stronger absorption (−52.9 dB to −35.3 dB of Co/C, −22.6 dB of Fe/C) and broader bandwidth

Table 1
EMW absorption properties of previously reported pure Fe_3O_4, Fe_3O_4/C composites and this work.

Sample	Filling ratio	Optimal RL (dB)	Optimal Thickness (mm)	Bandwidth		Ref
				Thickness(mm)	RL < −10 dB(GHz)	
Fe_3O_4 nanoparticles	60 wt%	−21.2	6.0	2.0	3.6 (14.4—18.0)	[57]
Fe_3O_4 nanocrystals	30 vol%	−21.1	5.0	2.0	−	[58]
Fe_3O_4/C nanospindles	60 wt%	−36.5	5.0	2.0	2.3 (10.5—12.8)	[59]
porous Fe_3O_4 flower-like nanostructures	50 wt%	−28.3	2.0	2.0	3.8 (11.7—15.5)	[60]
core-shell Fe_3O_4/C composites	50 wt%	−36.5	5.0	2.0	3.7 (11.8—15.5)	[61]
Fe_3O_4/carbon core/shell nanorods	55 wt%	−27.9	2.0	2.0	5.0 (13.0—18.0)	[43]
Fe_3O_4/C nanotubes	66.7 wt%	−22.6	1.7	2.0	4.8 (11.4—16.2)	[62]
RGO- Fe_3O_4 composites	40 wt%	−26.4	4.0	2.0	2.8 (10.4—13.2)	[34]
MWCNT/Fe_3O_4 hybrid materials	70 wt%	−18.2	2.0	2.0	−	[63]
F6 in this work	40 wt%	**−52.9**	3.07	**3.07**	**4.64 (9.44—14.68)**	This
F7 in this work	40 wt%	**−45.4**	1.58	**1.58**	**3.12 (14.48—17.6)**	This

(4.64 GHz−4.2 GHz of Co/C, 3.0 GHz of Fe/C at the same thickness of 3.0 mm). These results indicate the magnetic NPC nanorods pyrolyzed at 600 °C present to be very promising as the EMW absorber.

It becomes obvious in Fig. 4e−h that the absorption peaks shifted toward high frequency range as the thickness decreases from 5.0 to 1.0 mm. Such a shift can be explained by using the quarter wavelength model [54]:

$$t_m = n\lambda/4 = nc \left/ \left(4fm\sqrt{|\mu_r||\varepsilon_r|} \right) \right. \tag{9}$$

in which n = 1, 3, 5, …, c is the light velocity, t_m and f_m represent the predicted thickness and matching frequency of the optimal RL peaks, respectively. Fig. 5a'-d' shows the dependent curves of t_m on f_m for three samples at a wavelength of $\lambda/4$, in which blue open stars denote the matching thickness directly obtained from the 2D RL curves in Fig. 5a−d. All the blue stars are observed to locate around the $t_m = \lambda/4$ curve, indicating excellent EMW absorption performances of the magnetic NPC nanorods in accordance with the quarter-wavelength cancellation (interface cancellation) model. When the absorbers satisfy the quarter-wavelength model, the EM waves reflected from air-absorber interfaces and absorber-metal surfaces are out of phase by 180°, leading to a disappearance of each other on the air-absorber surfaces [40,54]. However, the interface cancellation is restricted by thickness and frequency and an optimal RL peak can be obtained at a specific frequency. Thus, more investigations of the contributions to the enhanced EMW absorption should be conducted.

Dielectric tangent loss $((\tan\delta_E = \varepsilon''/\varepsilon'))$ and magnetic tangent loss $((\tan\delta_M = \mu''/\mu'))$ are calculated to reflect the attenuation mechanisms of the samples. The observed lowest $\tan \delta_E$ and $\tan \delta_M$ of F5 indicate the weakest magnetic and dielectric loss ability of all samples (Fig. 6a). Upon increasing the pyrolysis temperature, an enhanced dielectric loss ability is recorded (Fig. 6b, c, d). The larger $\tan \delta_E$ value than $\tan \delta_M$ over the whole frequency range for F6, F7, F8 suggests that the dielectric loss is the dominant contribution to EMW absorption for the magnetic NPC nanorods. To evaluate the EMW attenuation ability of the samples, the attenuation constant (α) was evaluated by the attenuation value, expressed by Equation (10) [54]:

$$\alpha = \frac{\sqrt{2}\pi f}{c} \sqrt{(\mu''\varepsilon'' - \mu'\varepsilon') + \sqrt{(\mu''\varepsilon'' - \mu'\varepsilon')^2 + (\mu'\varepsilon'' + \mu''\varepsilon')^2}} \tag{10}$$

The sample F5 possesses the smallest α value, indicating the weakest attenuation capacity (Fig. 6e). A similar α value of F6, F7 and F8 suggests a strong attenuation ability, in accordance with the results in Fig. 4. Apart from the magnetic loss and dielectric loss

ability, impedance matching between the incident EMW and free space ($|Z_{in}/Z_0|$) has been considered as another crucial factor in determining the EMW absorption performances. Fig. 6f exhibits the curves of $|Z_{in}/Z_0|$ values versus frequency from 1.0 to 18.0 GHz at the same thickness of 3.0 mm for all samples. As a result, low ε_r and μ_r values of F5 result in larger $|Z_{in}/Z_0|$ value than 1.0 while $|Z_{in}/Z_0|$ value remaining at 1 indicates perfect impedance matching. F6 possesses a proper $|Z_{in}/Z_0|$ range around 1.0 from 8 to 14 GHz, while F7 owns a $|Z_{in}/Z_0|$ value close to 1.0 from 7.0 to 10.0 GHz. Furthermore, large permittivity value of F8 endows it with a smaller $|Z_{in}/Z_0|$ value than 1.0. F7 can still maintain a strong absorbing ability, but the bandwidth is not as broad as F6, owing to a lower impedance matching level than F6. The extremely low ε'' of F5 results in the weakest dielectric loss capacity and the worst impedance matching level amongst the studied samples. In case of F8, a good attenuation can be achieved, whereas the quite large ε' and ε'' makes it possess a poor impedance matching. Overall, thanks to the strong attenuation ability and best impedance matching level, F6 shows the most distinctive EMW absorption performances.

Compared with the reported Fe_3O_4 based absorbers, the enhanced absorbing capability of the Fe-MOFs derived magnetic NPC nanorods can be summarized into two folds. On one hand, the magnetic NPC nanorods can fully utilize the synergistic effect of dielectric loss deriving from carbon and strong magnetic loss from magnetic components, giving rise to strong EMW attenuation ability and excellent impedance matching. On the other hand, the porous structure can effectively regulate the effective permittivity (ε_{eff}) and thus improve the impedance matching based on the Maxwell-Garnett (MG) theory [12]:

$$\varepsilon_{eff}^{MG} = \varepsilon_1 \frac{(\varepsilon_2 + 2\varepsilon_1) + 2p(\varepsilon_2 - \varepsilon_1)}{(\varepsilon_2 + 2\varepsilon_1) - p(\varepsilon_2 - \varepsilon_1)} \tag{11}$$

where ε_1 and ε_2 are the permittivity in the solid and gas state, respectively. P represents the volume fraction of gas state in the porous materials. With enhancing the pore volume, the permittivity of the composites can be tuned to an extent. In addition, the porous structure can contribute to enhanced EM wave attenuation capability by inducing polarization relaxations [12,65]. In summary, the facilely prepared magnetic NPC nanorods derived from iron based MOFs possess significant potential as superior and light weight absorber.

4. Conclusions

In summary, a series of rod-shape composites were synthesized with Fe-containing magnetic nanoparticles uniformly embedded into porous carbon through pyrolysis of iron-based MOFs. The
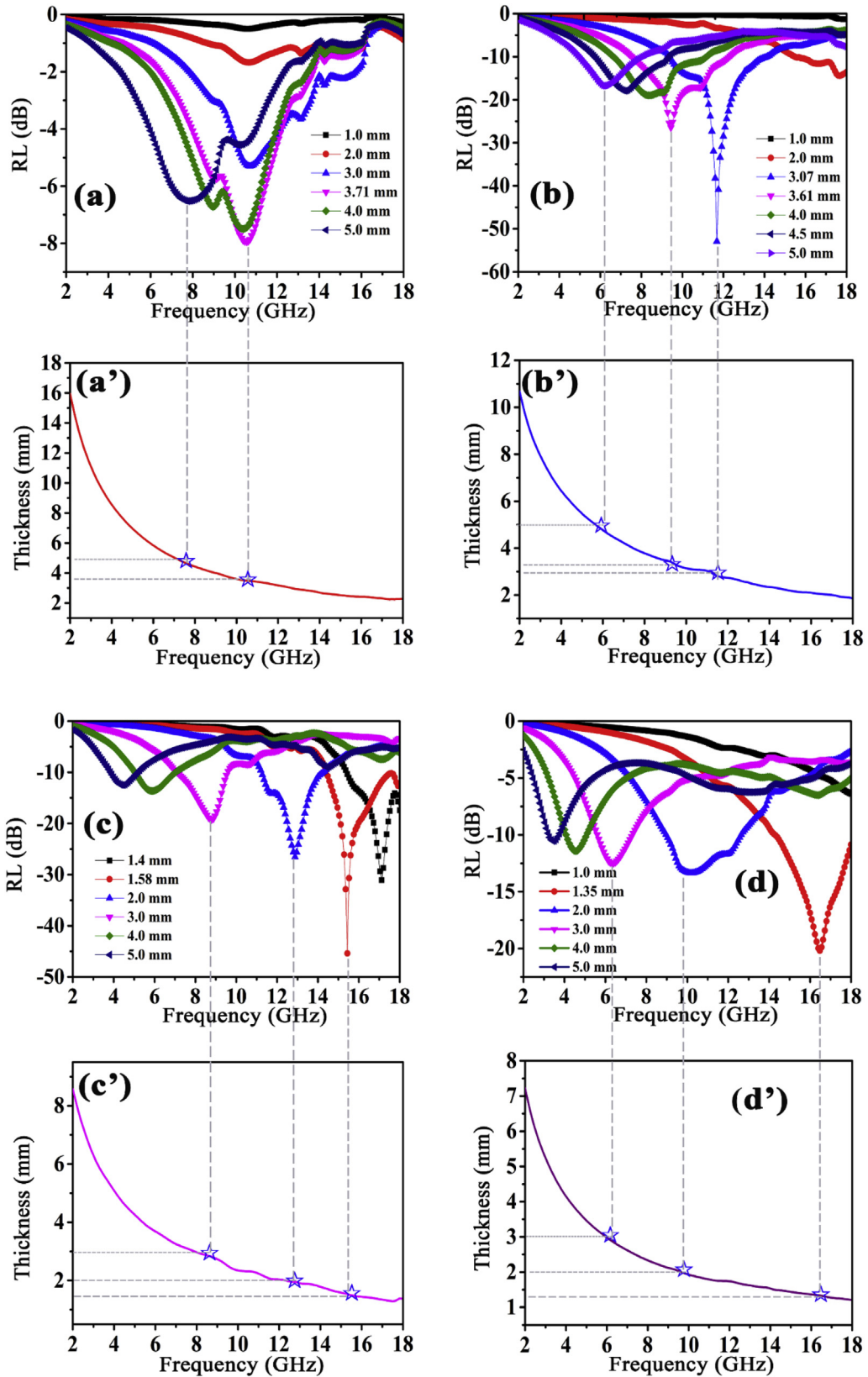
Fig. 5. Frequency dependence of RL values at different thicknesses (a-d) and (a'-d') dependence of matching thickness (t_m) on frequency for sample (a, a') F5, (b, b') F6 (c, c') F7 and (d, d') F8. (A colour version of this figure can be viewed online.)
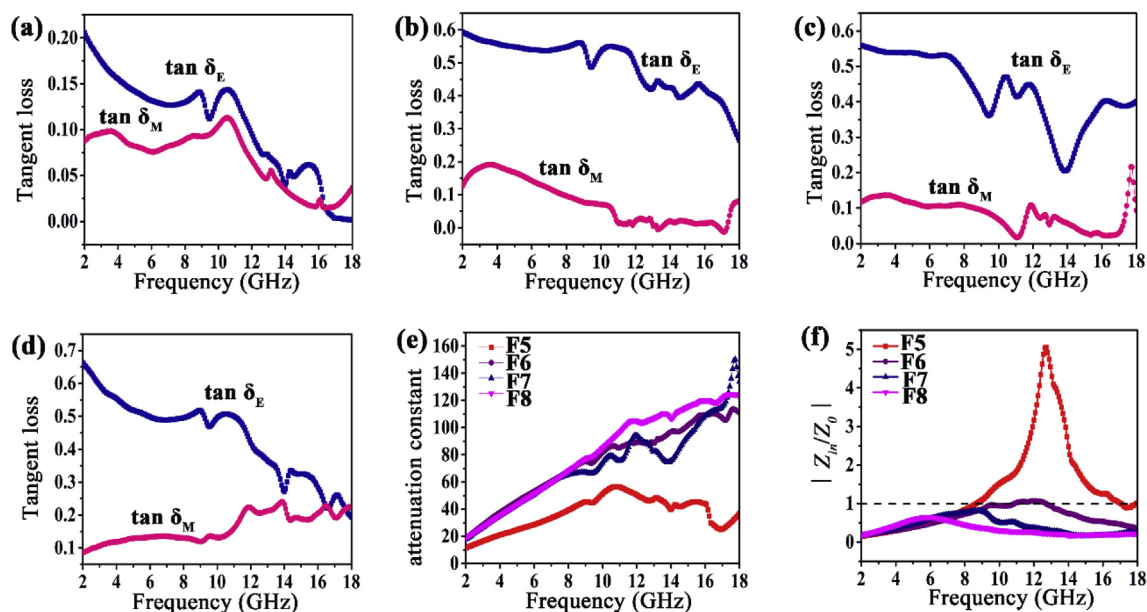
Fig. 6. Tangent loss for sample (a) F5, (b) F6, (c) F7, (d) F8. (e) Attenuation constant of the magnetic NPC nanorods pyrolyzed at different temperature. (f) Impedance match values for the magnetic NPC nanorods at the same thickness of 3.0 mm. (A colour version of this figure can be viewed online.)

morphology, compositions and graphitization of the magnetic NPC nanorods can be tuned by adjusting the pyrolysis temperatures. The graphitization degree can impact the permittivity level significantly. Too low graphitization at 500 °C caused a low permittivity while the formation of graphite carbon at 800 °C resulted in a largely increased permittivity, which could hardly satisfy an ideal absorber. The magnetic NPC nanorods pyrolyzed at 600 and 700 °C presented the most remarkable EMW absorption property with the minimum RL of −52.9 dB and −45.4 dB located at a thickness of 3.07 and 1.58 mm, and the effective bandwidth reached as large as 4.64 GHz for F6 and 3.12 GHz for F7. The complementary effects between multiple components, conduction loss, interface cancellation and highly porous structures contributed synergistically to the enhanced EMW absorption compared with previously reported Fe_3O_4 based absorbers, and MOFs-derived magnetic metals/carbon composites, which significantly improved the impedance matching. We believe those findings are shedding the light on elucidating the complex of materials properties towards the EMW absorption applications. Meanwhile, we believe this study will open the door for the applications of the MOFs-derived carbon/Fe_3O_4 composites in various other fields such as batteries and supercapacitors. In comparison with the heavy metals [66—72] and ceramics [73—77], and the less thermally stable polymers and their nanocomposites [78—81], the obtained magnetic carbon nanocomposites have other potential applications including polluted water treatments [82—85], energy storage/conversion [86,87], and multifunctional nanocomposites [88—91].

Appendix A. Supplementary data

Supplementary data to this article can be found online at https://doi.org/10.1016/j.carbon.2019.01.028.

References

[1] J. Guo, H. Song, H. Liu, C. Luo, Y. Ren, T. Ding, et al., Polypyrrole-interface-functionalized nano-magnetite epoxy nanocomposites as electromagnetic wave absorbers with enhanced flame retardancy, J. Mater. Chem. C 5 (2017) 5334—5344.

[2] C. Wang, V. Murugadoss, J. Kong, Z. He, X. Mai, Q. Shao, et al., Overview of carbon nanostructures and nanocomposites for electromagnetic wave shielding, Carbon 140 (2018) 696—733.

[3] L. Lv, J. Liu, C. Liang, J. Gu, H. Liu, H. Liu, et al., An overview of electrically conductive polymer nanocomposites toward electromagnetic interference shielding, Eng. Sci. 2 (2018) 26—42, https://doi.org/10.30919/es8d615.

[4] L. Kong, C. Wang, X. Yin, X. Fan, W. Wang, J. Huang, Electromagnetic wave absorption properties of a carbon nanotube modified by a tetrapyridinoporphyrazine interface layer, J. Mater. Chem. C 5 (2017) 7479—7488.

[5] L. Kong, X. Yin, X. Yuan, Y. Zhang, X. Liu, L. Cheng, et al., Electromagnetic wave absorption properties of graphene modified with carbon nanotube/poly(dimethyl siloxane) composites, Carbon 73 (2014) 185—193.

[6] L. Liu, S. Zhang, F. Yan, C. Li, C. Zhu, X. Zhang, et al., Three-dimensional hierarchical MoS₂ nanosheets/ultralong N-doped carbon nanotubes as high-performance electromagnetic wave absorbing material, ACS Appl. Mater. Interfaces 10 (2018) 14108—14115.

[7] Z. Wang, R. Wei, J. Gu, H. Liu, C. Liu, C. Luo, et al., Ultralight, highly compressible and fire-retardant graphene aerogel with self-adjustable electromagnetic wave absorption, Carbon 139 (2018) 1126—1135.

[8] H. Wu, X. Hu, L. Qian, Recent progress on the metacomposites with carbonaceous fillers, Eng. Sci. 2 (2018) 17—25, https://doi.org/10.30919/es8d735.

[9] B. Zhao, J. Deng, R. Zhang, L. Liang, B. Fan, Z. Bai, et al., Recent advances on the electromagnetic wave absorption properties of Ni based materials, Eng. Sci. 3 (2018) 5—40. www.doi.org/10.30919/es8d735.

[10] W. Liu, Q. Shao, G. Ji, X. Liang, Y. Cheng, B. Quan, et al., Metal−organic-frameworks derived porous carbon-wrapped Ni composites with optimized impedance matching as excellent lightweight electromagnetic wave absorber, Chem. Eng. J. 313 (2017) 734—744.

[11] D. Li, H. Liao, H. Kikuchi, T. Liu, Microporous Co@C nanoparticles prepared by dealloying CoAl@C precursors: achieving strong wideband microwave absorption via controlling carbon shell thickness, ACS Appl. Mater. Interfaces 9 (2017) 44704—44714.

[12] B. Quan, X. Liang, G. Ji, Y. Zhang, G. Xu, Y. Du, Cross-linking-derived synthesis of porous Co$_x$Ni$_y$/C nanocomposites for excellent electromagnetic behaviors, ACS Appl. Mater. Interfaces 9 (2017) 38814—38823.

[13] T. Wu, Y. Liu, X. Zeng, T. Cui, Y. Zhao, Y. Li, et al., Facile hydrothermal synthesis of Fe₃O₄/C core−shell nanorings for efficient low-frequency microwave absorption, ACS Appl. Mater. Interfaces 8 (2016) 7370−7380.

[14] N. Wu, J. Qiao, J. Liu, W. Du, D. Xu, W. Liu, Strengthened electromagnetic wave absorption performance derived from synergistic effect of carbon nanotube hybrid with Co@C beads, Adv. Compos. Hybrid. Mater. 1 (2018) 149−159.

[15] J. Xiang, J. Li, X. Zhang, Q. Ye, J. Xu, X. Shen, Magnetic carbon nanofibers containing uniformly dispersed Fe/Co/Ni nanoparticles as stable and high-performance electromagnetic wave absorbers, J. Mater. Chem. 2 (2014) 16905−16914.

[16] X. Zheng, J. Feng, Y. Zong, H. Miao, X. Hu, J. Bai, et al., Hydrophobic graphene nanosheets decorated by monodispersed superparamagnetic Fe₃O₄ nanocrystals as synergistic electromagnetic wave absorbers, J. Mater. Chem. C 3 (2015) 4452−4463.

[17] Z. Wang, L. Wu, J. Zhou, Z. Jiang, B. Shen, Chemoselectivity-induced multiple interfaces in MWCNT/Fe₃O₄@ZnO heterotrimers for whole X-band microwave absorption, Nanoscale 6 (2014) 12298−12302.

[18] X. Zhang, G. Ji, W. Liu, X. Zhang, Q. Gao, Y. Li, et al., A novel Co/TiO₂ nanocomposite derived from a metal−organic framework: synthesis and efficient microwave absorption, J. Mater. Chem. C 4 (2016) 1860−1870.

[19] R.C. Che, L.-M. Peng, X.F. Duan, Q. Chen, X.L. Liang, Microwave absorption enhancement and complex permittivity and permeability of Fe encapsulated within carbon nanotubes, Adv. Mater. 16 (2004) 401−405.

[20] L. Wang, T. Fei, Z. Lou, T. Zhang, Three-dimensional hierarchical flowerlike α-Fe₂O₃ nanostructures: synthesis and ethanol-sensing properties, ACS Appl. Mater. Interfaces 3 (2011) 4689−4694.

[21] Y. Yin, X. Liu, X. Wei, Y. Li, X. Nie, R. Yu, et al., Magnetically aligned Co−C/MWCNTs composite derived from MWCNT-interconnected zeolitic imidazolate frameworks for a lightweight and highly efficient electromagnetic wave absorber, ACS Appl. Mater. Interfaces 9 (2017) 30850−30861.

[22] G. Tong, W. Wu, Q. Hu, J. Yuan, R. Qiao, H. Qian, Enhanced electromagnetic characteristics of porous iron particles made by a facile corrosion technique, Mater. Chem. Phys. 132 (2012) 563−569.

[23] Z. Fang, C. Li, J. Sun, H. Zhang, J. Zhang, The electromagnetic characteristics of carbon foams, Carbon 45 (2007) 2873−2879.

[24] R. Qiang, Y. Du, D. Chen, W. Ma, Y. Wang, P. Xu, et al., Electromagnetic functionalized Co/C composites by in situ pyrolysis of metal-organic frameworks (ZIF-67), J. Alloy. Comp. 681 (2016) 384−393.

[25] W. Liu, L. Liu, Z. Yang, J. Xu, Y. Hou, G. Ji, A versatile route toward the electromagnetic functionalization of metal−organic framework-derived three-dimensional nanoporous carbon composites, ACS Appl. Mater. Interfaces 10 (2018) 8965−8975.

[26] K. Wang, Y. Chen, R. Tian, H. Li, Y. Zhou, H. Duan, et al., Porous Co−C core−shell nanocomposites derived from Co-MOF-74 with enhanced electromagnetic wave absorption performance, ACS Appl. Mater. Interfaces 10 (2018) 11333−11342.

[27] X. Liang, B. Quan, G. Ji, W. Liu, H. Zhao, S. Dai, et al., Tunable dielectric performance derived from the metal-organic-framework/reduced graphene oxide hybrid with broadband absorption, ACS Sustain. Chem. Eng. 5 (2017) 10570−10579.

[28] X. Zeng, Y. Bai, L. Zhu, H. Yang, R. Yu, Structure evolution of Prussian blue analogues to CoFe@C core-shell nanocomposites with good microwave absorbing performances, RSC Adv. 6 (2016) 105644−105652.

[29] H. Wang, F. Meng, J. Li, T. Li, Z. Chen, H. Luo, Carbonized design of hierarchical porous carbon/Fe₃O₄@Fe derived from loofah sponge to achieve tunable high-performance microwave absorption, ACS Sustain. Chem. Eng. 6 (2018) 11801−11810.

[30] Y. Lü, Y. Wang, H. Li, Y. Lin, Z. Jiang, Z. Xie, et al., MOF-derived Porous Co/C nanocomposites with excellent electromagnetic wave absorption properties, ACS Appl. Mater. Interfaces 7 (2015) 13604−13611.

[31] R. Qiang, Y. Du, H. Zhao, Y. Wang, C. Tian, Z. Li, et al., Metal organic framework-derived Fe/C nanocubes toward efficient microwave absorption, J. Mater. Chem. 3 (2015) 13426−13434.

[32] H. Lv, G. Ji, W. Liu, H. Zhang, Y. Du, P. Achieving hierarchical hollow carbon@Fe@Fe₃O₄ nanospheres with superior microwave absorption properties and lightweight features, J. Mater. Chem. C 3 (2015) 10232−10241.

[33] F. Wang, J. Liu, J. Kong, Z. Zhang, X. Wang, M. Itoh, et al., Template free synthesis and electromagnetic wave absorption properties of monodispersed hollow magnetite nano-spheres, J. Mater. Chem. 21 (2011) 4314.

[34] X. Sun, J. He, G. Li, J. Tang, T. Wang, Y. Guo, et al., Laminated magnetic graphene with enhanced electromagnetic wave absorption properties, J. Mater. Chem. C 1 (2013) 765−777.

[35] T. Chalati, P. Horcajada, R. Gref, P. Couvreur, C. Serre, Optimisation of the synthesis of MOF nanoparticles made of flexible porous iron fumarate MIL-88A, J. Mater. Chem. C 21 (2011) 2220−2227.

[36] P. Gao, R. Liu, H. Huang, X. Jia, H. Pan, MOF-templated controllable synthesis of α-Fe₂O₃ porous nanorods and their gas sensing properties, RSC Adv. 6 (2016) 94699−94705.

[37] K.-Y. Andrew Lin, H.-A. Chang, C.-J. Hsu, Iron-based metal organic framework, MIL-88A, as a heterogeneous persulfate catalyst for decolorization of Rhodamine B in water, RSC Adv. 5 (2015) 32520−32530.

[38] A.C. Ferrari, J. Robertson, Interpretation of Raman spectra of disordered and amorphous carbon, Phys. Rev. B 61 (2000) 14095−14107.

[39] R.O. Dillon, J.A. Woollam, Use of Raman scattering to investigate disorder and crystallite formation in as-deposited and anriealed carbon films, Phys. Rev. B 29 (1984) 3482−3489.

[40] Y. Yin, X. Liu, X. Wei, R. Yu, J. Shui, Porous CNTs/Co composite derived from zeolitic imidazolate framework: a lightweight, ultrathin, and highly efficient electromagnetic wave absorber, ACS Appl. Mater. Interfaces 8 (2016) 34686−34698.

[41] T. Wang, H. Wang, X. Chi, R. Li, J. Wang, Synthesis and microwave absorption properties of Fe−C nanofibers by electrospinning with disperse Fe nanoparticles parceled by carbon, Carbon 74 (2014) 312−318.

[42] S. Guo, J. Liu, S. Qiu, W. Liu, Y. Wang, N. Wu, et al., Porous ternary TiO₂/MnTiO₃@C hybrid microspheres as anode materials with enhanced electrochemical performances, J. Mater. Chem. 3 (2015) 23895−23904.

[43] Y.-J. Chen, G. Xiao, T.-S. Wang, Q.-Y. Ouyang, L.-H. Qi, Y. Ma, et al., Porous Fe₃O₄/carbon core/shell nanorods: synthesis and electromagnetic properties, J. Phys. Chem. C 115 (2011) 13603−13608.

[44] J. Liu, Y. Zhou, F. Liu, C. Liu, J. Wang, Y. Pan, et al., One-pot synthesis of mesoporous interconnected carbon-encapsulated Fe₃O₄ nanospheres as superior anodes for Li-ion batteries, RSC Adv. 2 (2012) 2262−2265.

[45] H. Lv, X. Liang, Y. Cheng, H. Zhang, D. Tang, B. Zhang, et al., Coin-like α-Fe₂O₃@CoFe₂O₄ core−shell composites with excellent electromagnetic absorption performance, ACS Appl. Mater. Interfaces 7 (2015) 4744−4750.

[46] S. Wei, X. Wang, B. Zhang, M. Yu, Y. Zheng, Y. Wang, et al., Preparation of hierarchical core-shell C@NiCo₂O₄@Fe₃O₄ composites for enhanced microwave absorption performance, Chem. Eng. J. 314 (2017) 477−487.

[47] J. Lv, X. Liang, G. Ji, B. Quan, W. Liu, Y. Du, Structural and carbonized design of 1D FeNi/C nanofibers with conductive network to optimize electromagnetic parameters and absorption abilities, ACS Sustain. Chem. Eng. 6 (2018) 7239−7249.

[48] Z. Li, X. Han, Y. Ma, D. Liu, Y. Wang, P. Xu, et al., MOFs-derived hollow Co/C microspheres with enhanced microwave absorption performance, ACS Sustain. Chem. Eng. 6 (2018) 8904−8913.

[49] X.G. Liu, J.J. Jiang, D.Y. Geng, B.Q. Li, Z. Han, W. Liu, et al., Dual nonlinear dielectric resonance and strong natural resonance in Ni/ZnO nanocapsules, Appl. Phys. Lett. 94 (2009), 053119.

[50] H. Wang, F. Meng, J. Li, T. Li, Z. Chen, H. Luo, Carbonized design of hierarchical porous carbon/Fe₃O₄@Fe derived from loofah sponge to achieve tunable high-performance microwave absorption, ACS Sustain. Chem. Eng. 6 (2018) 11801−11810.

[51] H. Wang, L. Xiang, W. Wei, J. An, J. He, C. Gong, et al., Efficient and lightweight electromagnetic wave absorber derived from metal organic framework-encapsulated cobalt nanoparticles, ACS Appl. Mater. Interfaces 9 (2017) 42102−42110.

[52] Y. Cheng, J. Cao, Y. Li, Z. Li, H. Zhao, G. Ji, et al., The outside-in approach to construct Fe₃O₄ nanocrystals/mesoporous carbon hollow spheres core−shell hybrids toward microwave absorption, ACS Sustain. Chem. Eng. 6 (2018) 1427−1435.

[53] M. Wu, Y.D. Zhang, S. Hui, T.D. Xiao, S. Ge, W.A. Hines, et al., Microwave magnetic properties of Co₅₀/(SiO₂)₅₀ nanoparticles, Appl. Phys. Lett. 80 (2002) 4404−4406.

[54] Z. Lou, H. Han, M. Zhou, J. Han, J. Cai, C. Huang, et al., Synthesis of magnetic wood with excellent and tunable electromagnetic wave-absorbing properties by a facile vacuum/pressure impregnation method, ACS Sustain. Chem. Eng. 6 (2018) 1000−1008.

[55] A. Aharoni, Effect of surface anistropy on the exchange resonance modes, J. Appl. Phys. 81 (1997) 830−833.

[56] P. Toneguzzo, G. Viau, O. Acher, F. Fievet-Vincent, F. Fievet, Monodisperse ferromagnetic particles for microwave applications, Adv. Mater. 10 (1998) 1032−1035.

[57] G. Wang, Y. Chang, L. Wang, L. Liu, C. Liu, Facilely preparation and microwave absorption properties of Fe₃O₄ nanoparticles, Mater. Res. Bull. 48 (2013) 1007−1012.

[58] S. Ni, S. Lin, Q. Pan, F. Yang, K. Huang, D. He, Hydrothermal synthesis and microwave absorption properties of Fe₃O₄ nanocrystals, J. Phys. D Appl. Phys. 42 (2009), 055004.

[59] X. Liu, X. Cui, Y. Chen, X.-J. Zhang, R. Yu, G.-S. Wang, et al., Modulation of electromagnetic wave absorption by carbon shell thickness in carbon encapsulated magnetite nanospindles−poly(vinylidene fluoride) composites, Carbon 95 (2015) 870−878.

[60] X. Li, B. Zhang, C. Ju, X. Han, Y. Du, P. Xu, Morphology-controlled synthesis and electromagnetic properties of porous Fe₃O₄ nanostructures from iron alkoxide precursors, J. Phys. Chem. C 115 (2011) 12350−12357.

[61] Y. Du, W. Liu, R. Qiang, Y. Wang, X. Han, J. Ma, Shell thickness-dependent microwave absorption of core−shell Fe₃O₄@C composites, ACS Appl. Mater. Interfaces 6 (2014) 12997−13006.

[62] W. Li, B. Lv, L. Wang, G. Li, Y. Xu, Fabrication of Fe₃O₄@C core−shell nanotubes and their application as a lightweight microwave absorbent, RSC Adv. 4 (2014) 55738−55744.

[63] C. Hou, T. Li, T. Zhao, H. Liu, L. Liu, W. Zhang, Electromagnetic wave absorbing properties of multi-wall carbon nanotube/Fe₃O₄ hybrid materials, N. Carbon Mater. 28 (2013) 184−190.

[64] J.R. Liu, M. Itoh, K. Machida, Magnetic and electromagnetic wave absorption properties of α-Fe/Z-type Ba-ferrite nanocomposites, Appl. Phys. Lett. 88 (2006), 062503.

[65] H. Xu, X. Yin, M. Zhu, M. Han, Z. Hou, X. Li, et al., Carbon hollow microspheres with a designable mesoporous shell for high-performance electromagnetic wave absorption, ACS Appl. Mater. Interfaces 9 (2017) 6332−6341.

[66] Z. Zhao, R. Guan, J. Zhang, Z. Zhao, P. Bai, Effects of process parameters of semisolid stirring on microstructure of Mg-3Sn-1Mn-3SiC (wt%) strip processed by rheo-rolling, Acta Metall. Sin. 30 (2017) 66−72.

[67] Z. Zhao, P. Bai1, R. Guan, V. Murugadoss, H. Liu, X. Wang, Z. Guo, Microstructural evolution and mechanical strengthening mechanism of Mg-3Sn-1Mn-1La alloy after heat treatments, Mater. Sci. Eng., A 734 (2018) 200−209.

[68] Z. Zhao, R. Misra, P. Bai, J. Gao, Y. Li, R. Guan, Z. Guo, Novel process of coating Al on graphene involving organic aluminum accompanying microstructure evolution, Mater. Lett. 232 (2018) 202−205.

[69] Y. Zhao, L. Qi, Y. Jin, K. Wang, J. Tian, P. Han, The structural, elastic, electronic properties and Debye temperature of D022-Ni3V under pressure from first-principles, J. Alloy. Comp. 647 (2015) 1104−1110.

[70] Y. Zhao, B. Zhang, H. Hou, W. Chen, M. Wang, Phase-field simulation for the evolution of solid/liquid interface front in directional solidification process, J. Mater. Sci. Technol. (2019), https://doi.org/10.1016/j.jmst.2018.12.009 in press.

[71] Y. Zhao, S. Deng, H. Liu, J. Zhang, Z. Guo, H. Hou, First-principle investigation of pressure and temperature influence on structural, mechanical and thermodynamic properties of Ti_3AC_2 (A=Al and Si), Comput. Mater. Sci. 154 (2018) 365−370.

[72] Y. Zhao, X. Tian, B. Zhao, Y. Sun, H. Guo, M. Dong, et al., Precipitation sequence of middle Al concentration alloy using the inversion algorithm and microscopic phase field model, Sci. Adv. Mater. 10 (2018) 1793−1804.

[73] Z. Qu, M. Shi, H. Wu, Y. Liu, J. Jiang, C. Yan, An efficient binder-free electrode with multiple carbonized channels wrapped by $NiCo_2O_4$ nanosheets for high-performance capacitive energy storage, J. Power Sources 410−411 (2019) 179−187.

[74] B. Kirubasankar, V. Murugadoss, J. Lin, T. Ding, M. Dong, H. Liu, et al., In-situ grown nickel selenide onto graphene nanohybrid electrodes for high energy density asymmetric supercapacitors, Nanoscale 10 (2018) 20414−20425.

[75] Y. Sheng, J. Yang, F. Wang, L. Liu, H. Liu, C. Yan, Z. Guo, Sol-gel synthesized hexagonal boron nitride/titania nanocomposites with enhanced photocatalytic activity, Appl. Surf. Sci. 465 (2019) 154−163.

[76] W. Du, X. Wang, J. Zhan, X. Sun, L. Kang, F. Jiang, et al., Biological cell template synthesis of nitrogen-doped porous hollow carbon spheres/MnO_2 composites for high-performance asymmetric supercapacitors, Electrochim. Acta 296 (2019) 907−915.

[77] M. Idrees, S. Batool, J. Kong, Q. Zhuang, H. Liu, Q. Shao, et al., Polyborosilazane derived ceramics - nitrogen sulfur dual doped graphene nanocomposite anode for enhanced lithium ion batteries, Electrochim. Acta 296 (2019) 925−937.

[78] C. Wang, Z. He, X. Xie, X. Mai, Y. Li, T. Li, et al., Controllable cross-linking anion exchange membranes with excellent mechanical and thermal properties, Macromol. Mater. Eng. 3 (2018) 1700462.

[79] D. Jiang, V. Murugadoss, Y. Wang, J. Lin, T. Ding, Z. Wang, et al., Electromagnetic interference shielding polymers and nanocomposites − a review, Polym. Rev. (2019), https://doi.org/10.1080/15583724.2018.1546737 in press.

[80] C. Wang, B. Mo, Z. He, C.X. Zhao, L. Zhang, Q. Shao, et al., Hydroxide ions transportation in polynorbornene anion exchange membrane, Polymer 138 (2018) 363−368.

[81] C. Wang, B. Mo, Z. He, Q. Shao, D. Pan, E. Wujick, et al., Crosslinked norbornene copolymer anion exchange membrane for fuel cells, J. Membr. Sci. 556 (2018) 118−125.

[82] Z. Zhao, H. An, J. Lin, M. Feng, V. Murugadoss, T. Ding, et al., Progress on the photocatalytic reduction removal of chromium contamination, Chem. Rec. 18 (2018) 1−11, https://doi.org/10.1002/tcr.201800153.

[83] Z. Li, B. Wang, X. Qin, Y. Wang, C. Liu, Q. Shao, et al., Superhydrophobic/superoleophilic polycarbonate/carbon nanotubes porous monolith for selective oil adsorption from water, ACS Sustain. Chem. Eng. 6 (2018) 13747−13755.

[84] Y. Qian, Y. Yuan, H. Wang, H. Liu, J. Zhang, S. Shi, Z. Guo, N. Wang, Highly efficient uranium adsorption by salicylaldoxime/polydopamine graphene oxide nanocomposites, J. Mater. Chem. 6 (2018) 24676−24685.

[85] J. Huang, Y. Li, Y. Cao, F. Peng, Y. Cao, Q. Shao, H. Liu, Z. Guo, Hexavalent chromium removal over magnetic carbon nanoadsorbent: synergistic effect of fluorine and nitrogen co-doping, J. Mater. Chem. 6 (2018) 13062−13074.

[86] H. Du, C. Zhao, J. Lin, Z. Hu, Q. Shao, J. Guo, et al., Carbon nanomaterials in direct liquid fuel cells, Chem. Rec. 18 (2018) 1365−1372.

[87] T. Su, Q. Shao, Z. Qin, Z. Guo, Z. Wu, Role of interfaces in two-dimensional photocatalyst for water splitting, ACS Catal. 8 (2018) 2253−2276.

[88] H. Wei, H. Wang, Y. Xia, D. Cui, Y. Shi, M. Dong, et al., An overview of lead-free piezoelectric materials and devices, J. Mater. Chem. C 6 (2018) 12446−12467.

[89] H. Liu, Q. Li, S. Zhang, R. Yin, X. Liu, Y. He, et al., Electrically conductive polymer composites for smart flexible strain sensor: a critical review, J. Mater. Chem. C 6 (2018) 12121−12141.

[90] N. Wu, C. Liu, D. Xu, J. Liu, W. Liu, Q. Shao, Z. Guo, Enhanced electromagnetic wave absorption of three-dimensional porous Fe_3O_4/C composite flowers, ACS Sustain. Chem. Eng. 6 (2018) 12471−12480.

[91] Z. Wang, H. Zhu, N. Cao, R. Du, Y. Liu, G. Zhao, Superhydrophobic surfaces with excellent abrasion resistance based on benzoxazine/mesoporous SiO_2, Mater. Lett. 186 (2017) 274−278.